International Journal of Material Forming (2023) 16:52
https://doi.org/10.1007/s12289-023-01776-x

ORIGINAL RESEARCH

Improvements in elongation and tradeoffs in strength and ductility of several Mg sheet alloys through cyclic bending under tension and annealing

Nikolai Matukhno[1] · Nemanja Kljestan[1] · Sven C. Vogel[2] · Marko Knezevic[1]

Received: 10 March 2023 / Accepted: 19 July 2023

Abstract
This paper presents results acquired from experimental investigations into determining the influence of cyclic-bending-under-tension (CBT) and annealing on elongation-to-fracture (ETF) and tradeoffs in strength and ductility of three Mg sheet alloys: ZEK100, BioMg250, and Mg4Li. The CBT process imparts uniform deformation greater than achievable in simple tension (ST) incrementally by subjecting a sheet specimen to simultaneous tension with a crosshead motion and bending with a set of rollers reciprocating along the specimen. The space of process parameters including crosshead velocity and bending depth is explored initially to achieve the greatest ETF of ZEK100 alloy. Improvements in ETF of about 40% are attained using CBT relative to ST. Given the uniform deformation imparted by CBT to large plastic strains, tradeoffs in strength and ductility of the alloy are investigated next by subjecting the alloy sheets to a certain number of CBT cycles under the optimized parameters and subsequent annealing. Strength of the alloy is found to increase by a factor of 1.4 along the sheet strongest direction, the rolling direction, and a factor of 2 along the sheet softest direction, the transverse direction. Since the strength improved more along the soft direction than along the hard direction, the alloy anisotropy reduces. Significantly, the strength can increase for about 40% along the soft direction, while reducing the anisotropy and preserving at least 10% of the alloy ductility in every direction. Characterization of microstructural evolution using electron-backscattered diffraction and texture evolution using neutron diffraction revealed slip dominated deformation of the alloy. Similar processing and testing of BioMg250 and Mg4Li sheet alloys produced even better results in terms of enhancing elongation and improving the contrasting strength and ductility properties. Comprehensive data for the three alloys and insights from the investigations are presented and discussed.

Keywords Elongation · Strength · Microstructures · Cyclic-bending-under-tension · Mg sheet alloys

Introduction

Reducing structural weight, termed ‘lightweighting’, is a strategy to reduce consumption of fossil fuels in transportation industries [1]. Magnesium (Mg) alloys are being more and more evaluated in such efforts because of their low density and high specific strength, in addition to their good castability, weldability, and machinability [2, 3]. Mg alloys also meet the design challenges important to consumer electronics needing to become lighter and thinner [4]. For the treatment of fractures of bones, orthopedic implants made of steel or titanium are usually used when weight-bearing bones are impacted. The major drawback of such metallic implants is that they must to be removed [5]. Resorbable metallic implants like those of Mg alloys are crucial that complementarily provide adequate stability for weight-bearing applications [6]. However, Mg alloys suffer from inadequate ductility preventing their shaping at room temperature [7–9]. Poor formability of Mg alloys at room temperature is associated with their hexagonal closed-packed (HCP) crystal structure and underlying abundant twinning and difficulties to activate enough slip systems (basal, prismatic, and pyramidal modes of slip) for

✉ Marko Knezevic
marko.knezevic@unh.edu

[1] Department of Mechanical Engineering, University of New Hampshire, 33 Academic Way, Kingsbury Hall, W119, Durham, NH 03824, USA

[2] Materials Science and Technology Division, Los Alamos National Laboratory, Los Alamos, NM 87545, USA

Published online: 31 July 2023

accommodating large plastic strains [10–14]. Forming at high temperatures improves the formability of Mg alloys but comes with accompanying cost [15–18].

Relationships between mechanical response of metals concerning strength/work hardening/formability and microstructure have been widely studied [19–23]. Solid solution hardening, precipitation hardening, grain size refinement strengthening, and cold-work strengthening are the key ways to improve strength of Mg alloys [24, 25]. Substantial improvements in ductility were achieved by alloying with rare earth (RE) elements (e.g. Y, Gd, and Ce) and underlying altering of crystallographic texture to increase activity of non-basal slip systems [26–29]. Alloying with RE elements and long processing and/or heat treatment times to obtain favorable strength versus ductility compromises are also costly [30–33].

Plastic instabilities i.e. necking develop in sheets during forming restricting the plastic deformation in the localized neck regions until ultimate fracture at that location. As an alternative to the development of advanced alloys for enhanced elongation-to-fracture (ETF) or displacement at fracture and possible lowered energy consumption pertains to innovations in sheet metal forming operations, which change the deformation history experienced by the sheet undergoing forming [34]. Amounts of plastic deformation beyond conventional forming limits usually described by forming limit diagrams can be achieved using incremental sheet forming, where a small volume of the material is plastically deforming at each instant [35]. Similarly, a tool imparts an incremental deformation over a spinning blank to form an axisymmetric part using a spin forming process [36]. Drawbeads often used in forming of sheets can also increase ETF [37]. In all these processes the sheet experiences simultaneously an amount of bending under tension [38]. The fact that bending, as a stabilizing mechanism, can improve ETF has been known for long time [39]. Tool radius and sheet thickness have been observed to play a role on ETF in bending tests [40]. Taking advantages of bending under stretching, improvements in ETF of Mg alloy AZ31 were achieved via a cross-wavy process of bending [41], a continuous process of V-bending [42], and a continuous bending channel couples with an equal-channel-angular-rolling [43]. To take advantage of both the incremental forming aspects of enhancing ETF and the stabilizing mechanism of bending enhancing EFT more explicitly, a cyclic bending under tension (CBT) test/process has been conceived to imparts cyclic bending during tension of sheets [44–46]. In particular, the innovation attempts to exploit the intrinsic ETF throughout the sheet, while delaying necking and fracture that the necking causes [47]. Outside of the actual necked region, a sheet has ample of idle ductility, which the CBT process can exploit.

The greatest improvements in ETF using CBT were observed for alloys that exhibit necking in simple tension (ST) such as dual-phase steels [48] and Al alloys [49]. Moderate improvements were obtained for alloys failing with small necking such as AZ31 [50]. Importantly, the CBT process facilitates studying microstructural evolution in sheets after tension at strains greater than those possible to achieve in ST. To this end, cellular dislocation structures in Al alloys [51] and dislocation tangles in steels [52] were characterized after CBT processing. Given that strain levels in many sheet metal forming operations are greater than those attainable in ST [53], the post-necking sheet behavior is usually approximated using a selected phenomenological hardening law [54]. Nevertheless, various methods for determining the actual stress-strain response of sheets beyond necking are being explored [55] to improve accuracy of metal forming simulations [56]. To this end, an additional benefit of the CBT test pertains to inferring the post-necking work hardening behavior of sheets [57]. The approach involves CBT testing and the finite element method (FEM) simulations of the recorded load versus displacement data [58]. The approach comes with an assumption that the stress/strain state in CBT closely resembles that in ST [59].

Figure 1 illustrates the process schematically. A constant pulling velocity is applied at one end of a sheet specimen, while the other end is fixed. The resulting axial tensile force ensures sufficient wrapping of the sheet around the rollers for the plastic flow over the rollers. A set of three rollers move from one end of the specimen gauge section to the other imparting continuous bending/unbending of the sheet specimen under tension. The rollers engage incrementally a region by region of the sheet specimen with their axial motion. The moving region is a deformation zone in which the sheet experiences a combination of plastic bending and tension periodically. The deformation zone is exclusively underneath the rollers, while the rest of the sheet is in tension elastically. The separation of the specimen gauge section into the plastically deforming regions underneath the rollers

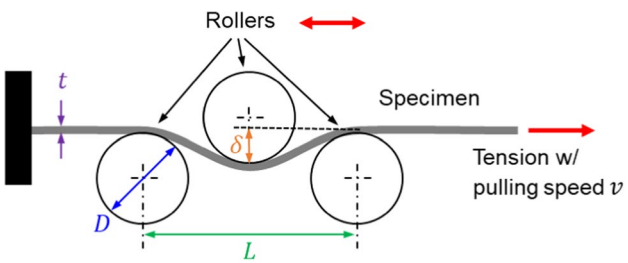

Fig. 1 Schematic illustration of the CBT process highlighting several geometric features: the bending depth (δ) set by moving the top roller up and down, fixed distance between the bottom rollers ($L = 54$ mm), fixed diameter of the rollers ($D = 25.4$ mm), and thickness of the sheet undergoing CBT (t)

that move axially from the rest of the elastically deforming specimen facilitates uniform elongation of the sheet to larger plastic strains than those attainable in ST before necking. The uniform deformation of the gauge section in CBT is much greater than in ST. Essentially, ductility is depleted throughout the specimen gauge length circumventing necking at a single region intrinsic to ST followed by fracture. The hardening is therefore relatively uniform throughout the sheet gauge section until localization and fracture, as opposed to taking place in the neck after the uniform elongation is exhausted in ST. At the necking event, rest of the specimen unloads with ample of remaining ductility. In contrast, CBT exploits such ductility. Because of hardening, the axial stress/strain increases during the CBT test, even though the bending stress/strain imposed over the deformation zone remains constant. Therefore, the elastic stress/strain in the sheet grow with CBT.

This paper is a second study into the effects of CBT on ETF of Mg sheet alloys. The first study involved alloy AZ31 [50]. Here, results are presented for three additional alloys: a 1.4 mm rolled RE Mg alloy, ZEK100 [60], a 2 mm rolled biocompatible Mg alloy, BioMg250 [61], and, the lightest and softest of all Mg alloys, a 1.6 mm extruded Mg alloy, Mg4Li [62]. The studied alloys had different thicknesses important for bending, in addition to the manufacturing technique used to produce them and their chemical compositions. The parameter space including crosshead velocity and bending depth was first explored to achieve the greatest ETF of ZEK100 sheets relative to ST along three sheet directions. Force versus displacement curves as a function of these parameters are presented and described. Moreover, the study sought the tradeoffs in strength and ductility for the alloy by performing annealing after uniform pre-straining in CBT to selected number of CBT cycles. The test direction and underlying anisotropy were found to play an important role in establishing the tradeoffs. In addition to processing and testing, a combination of electron-backscattered diffraction (EBSD) and neutron diffraction was employed to characterize the initial grain structure and crystallographic texture and microstructural evolution of the alloy subjected to ST, CBT, and annealing. Microstructural evolution observations facilitated a discussion of deformation mechanisms accommodating the plastic strains in the alloy. Finally, similar processing and testing of sheets of BioMg250 and sheets of Mg4Li were performed. The established testing procedures and parameters for ZEK100 were used to reduce the number of tests performed on BioMg250 and Mg4Li alloys. Comprehensive results for the three alloys in terms of improving their elongation with CBT and enhancing their strength and residual ductility with CBT and annealing are presented and discussed in this paper.

Table 1 Chemical composition of ZEK100-O (wt%)

	Zn	Nd	Zr	Mn	Mg
ZEK100-O	1.3	0.2	0.25	0.01	Balance

Mg alloys and experiments

This section describes the studied alloys and experimental procedures used in testing and processing of the alloys.

Mg alloys

Premier examples of advanced Mg alloys are selected for the study. The first alloy is a RE Mg alloy, ZEK100 offers good ductility over many other conventional Mg alloys at room temperature but suffers from significant anisotropy and relatively complex yield behavior. The second alloy is a RE- and Al-free, high strength dilute Mg alloy, BioMg250, aimed at biomedical applications. The third alloy is the lightest and the softest of all structural Mg alloys, Mg4Li, which can greatly benefit from strengthening while preserving some residual ductility.

Rolled sheets of a commercial RE Mg ZEK100-O alloy with a nominal thickness of 1.4 mm were produced at Magnesium Elektron Inc [60]. The same alloy used in the present work was used in another low cycle fatigue study [63]. The alloy was in O-temper condition meaning that the alloy underwent annealing to remove any cold work. The chemical composition of the alloy is provided in Table 1.

BioMg250 sheets were made by hot rolling the as-cast ingots of composition presented in Table 2 to thickness of 2.0 mm. Prior to CBT, the sheets were annealed at 400 °C for 1 h to ensure the annealed condition [64].

Cast billets of the chemical composition presented in Table 3 were extruded into sheets with an extrusion ratio of R = 61:1 at 300 °C [62]. The sheets had a thickness of 1.6 mm and were tested in the as-extruded condition.

Testing

Monotonic ST and strain rate ST jump tests were performed first. Specimens for these tests had a gauge length of 50 mm and width of 12.5 mm. Next, CBT testing was performed.

Table 2 Chemical composition of BioMg250 (wt%)

	Zn	Ca	Mn	Mg
BioMg250	1.3	0.4	0.4	Balance

Table 3 Chemical composition of Mg4Li (wt%)

	Li	Mg
Mg4Li	4	Balance

Figure 2 shows a drawing of a specimen used in CBT testing. The specimen is a suitably lengthened ASTM E8 tensile specimen such that the rollers never leave the gauge section. The deformation regions, 1x, 2x, and 3x, based on the number of banding cycles are indicated in the figure. Last, secondary ST testing was performed using sub-size specimens. These specimens had a gauge length of 32 mm and width of 6 mm, also according to ASTM E8 [65]. These specimens were cut from CBT processed specimens interrupted after a certain number of CBT cycles, as shown in Fig. 2. The specimens were from the 3x region of the CBT specimens. The secondary tests were used to evaluate residual ductility and enhancement in strength of the CBT processed sheets. Making the specimens was by water jet as slightly oversized and then machining by a 3-axis CNC machine to the dimensions. Testing was performed along the rolling direction (0° or RD), diagonal direction (45° or DD) and transverse direction (90° or TD) for ZEK100 and BioMg250, while along the extruded direction (ED) and normal to ED (NED) for Mg4Li sheet.

The strain rate ST jump tests were performed to assess any appreciable strain rate sensitivity (SRS) of the alloys because strain rates vary in a small range during CBT. To this end, the jumps from 0.0001/s to 0.001/s, m_1, from 0.001/s to 0.01/s, m_2, and from 0.01/s to 0.1/s, m_3 were tested. SRS: $m = {}^{ln\frac{\sigma_2}{\sigma_1}}\Big/_{ln\frac{\epsilon_2}{\epsilon_1}}$ was calculated from the data, where 1 and 2 represent strain and stress values per jump.

An MTS Landmark 370 servo hydraulic mechanical testing machine involving Flextest software and controller was used to test the materials [66–68]. The machine is equipped with a pair of hydraulic grips for clamping test specimens. An MTS 632.12 F-20 extensometer was used to acquire displacement in combination with the displacement of the actuator for cross verification. The tests were performed at a nominal strain rate of 10^{-3} s^{-1} and room temperature to breaking.

A CBT experimental apparatus available at the University of New Hampshire is shown in the Appendix 1, while more details were presented in [69]. Briefly, the apparatus has the moving carriage (including a specimen, the grips, two load cells (one on each grip) and a hydraulic actuator), the fixed roller assembly located on the base, the bed (including an AC brushless servomotor and a ball screw connected to the carriage which is used for moving it) and the hardware/software for data-collection. The carriage holds a hydraulic actuator rated for 310 kN with a stroke of 305 mm. The actuator has a Micropulse BTL7-A501-M0305-Z-S23 position sensor (Balluff, Neuhausen, Germany) with a resolution of 5 µm and is connected to an 11.2 kW high-pressure hydraulic pump of 32 L/min and 210 bar capacity. Two donut-style load-cells, the first one is for tension (LCF450, capacity of 22.24 kN, Futek, Irvin, CA, USA) and the second one is for compression (LTH500, capacity of 22.24 kN, Futek, Irvin, CA,USA) are attached to the actuator and the carriage, respectively. The Sheffer HH Series hydraulic cylinder is fitted with a Balluff BTL7 MicroPulse + displacement and velocity sensor. The sensor uses a magneto-strictive principle, in which the mechanical motion of a magnet produces a potential. This voltage is proportional to the cylinder rod's position and velocity. The BLT7 MicroPulse + uses a 24 V supply, and provides 10 V analog output signal. The signal resolution is less than 0.33 mV, with 5 µm of hysteresis, and a maximum sampling rate of 4 kHz. The roller-assembly is made of three stainless-steel rollers of 25 mm diameter which are supported on self-aligning, spherical sliding bearings. The moving carriage and roller assembly are connected to a cast iron bed, which also houses a 1 kW AC brushless servomotor and a ball screw. The nut of the ball screw is connected to the bottom of the carriage, setting the latter to a reciprocating motion during the CBT tests. A program created in LabVIEW is used for control and data-acquisition. The system collects the axial loads from the load cells, velocity of the carriage, and crosshead displacement.

The specimen is held between two wedge-type grips. The carriage runs with a fixed velocity of 66 m/s. After motion to the end of the stroke in one direction, the carriage receives a signal from a limit switch to reverse. One of two limit switches is connected to the roller assembly. Another limit switch is placed on the moving crosshead because the specimen is elongating during CBT. For clarity, rollers describe a CBT pass by traversing the gauge length from one side to the other, while rollers describe a CBT cycle by additionally traversing the gauge length back from the other side to the original side. Furthermore, for clarity, the region of the specimen close to the grips undergoing CBT bends/unbends

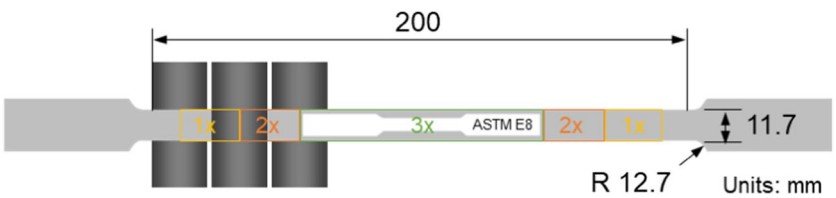

Fig. 2 Drawing of an initial CBT specimen containing a subsize specimen with a gauge section of 32 mm in length and 6 mm in width for subsequent ST. The deformation regions, 1×, 2×, and 3×, are indicated approximately

once per pass (1x), while the central region bends/unbends three times leading to a uniformly deformed region (3x). The CBT process parameters are bending depth and crosshead speed. The bending stress/strain state along with the tensile stress/strain state in a CBT test induces a non-symmetric overall tension/compression stress/strain profile, with the neutral axis cyclically moving towards the surface of the sheet.

Annealing

A set of samples processed by CBT was annealed to restore their ductility. The annealing setup included a Carbolite Gero GPCMA/37 furnace with a 3504 controller. A plate made of ceramic was used to inhibit conductive heat transfer between the bottom of the furnace and the specimen. Chamber of the furnace was preheated to the desired temperature prior placing specimens inside the furnace. After one hour of HT, the specimens are air-cooled to room temperature. K-type thermocouple was used to monitor and record the temperature inside the chamber. The alloy ZEK100 anneals fully at 400 °C for 1 h. Therefor, 100 °C, 200 and 300 °C are chosen as partial annealing temperatures for ZEK100. Mg4Li was extruded at 300 °C. Such dynamic regime actually anneals the alloy. The same temperature range was chosen for Mg4Li as for ZEK100. BioMg250 did not show signs of recovery at 200 °C. Therefore, 250 °C is chosen as the minimum temperature for annealing BioMg250. All specimens were held for one hour inside the furnace at the temperatures.

Characterization

EBSD characterization of the alloys was performed employing a Pegasus system (Hikari High-Speed Camera and Octane Plus SDD detector) attached to a Tescan Lyra (Ga) scanning electron microscope (SEM).

Samples of ZEK100 were first sanded using SiC papers of 400 grit, then polished with oil-based diamond suspension of 9, 3, and 1 µm on TexMet C cloths, and mirror finished using MastePolish (0.05 µm colodial silica + alumina) & ethylene glycol (1:1 ratio) on a ChemoMet pad. The polished samples were finally etched using 60% ethanol, 15% acetic acid, 20% distilled water, 5% nitric acid for 3–8 s, depending on the straining condition. Step size for the scans was 0.25 µm. The scans were taken under 22 kV.

Samples of BioMg250 were ground on SiC papers 400 to 4000 grit under running water, polished with oil-based diamond suspensions of 3 and 1 µm on cloths, and finally polished with colloidal silica to mirror finish. Step size for the scans was 0.25 µm. The scans were taken under 22 kV.

Samples of Mg4Li were first sanded using SiC papers of 800 grit, then polished with oil-based diamond suspension of 9, 3, and 1 µm on TexMet C cloths, and mirror finished using MastePolish (0.05 µm colodial silica + alumina) & ethylene glycol (1:1 ratio) on a ChemoMet pad. The polished samples were finally etched using 60% ethanol, 15% acetic acid, 20% distilled water, 5% nitric acid for 3–8 s, depending on the straining condition. Step size for the scans was 0.25 µm. The scans were taken under 22 kV.

All samples were cleaned in ethyl-alcohol for 4 to 5 min in an ultrasonic bath after polishing.

Neutron diffraction was performed at the High Pressure Preferred Orientation beam-line at Los Alamos National Laboratory [70]. This neutron diffractometer was used to measure macroscopic bulk texture. Count times were equivalent to approximately 30 min at a proton current of 100 micro-A. Inverse pole figures (IPFs) were measured in 135 sample directions ensuring the coverage to fit an orientation distribution functions in the Rietveld refinement of the 135 patterns, including the structural parameters such as lattice parameters and/or weight fractions [71–73]. Rietveld refined orientation distribution functions was used to obtain corresponding pole figures per sample. The orientation distribution function analysis of the data was done using MAUD [71] with 7.5° resolution. Plotting of the pole figures was done in MTEX [74].

Results

Figure 3a shows stress-strain curves measured for the as-received sheets of ZEK100. The alloy shows a great deal of tensile plastic anisotropy with RD as the strongest and TD as the softest planar direction. The uniform elongation of the alloy along the strongest direction is just above 10%. The hardening is more rapid along the softer TD than along the harder RD, while the 45° direction is in between. Basic properties taken from the curves are provided in the Appendix 1. Evidently, the elongation is a strong function of the orientation. Inspection of several specimens tested to fracture under ST revealed that only a small amount of necking occurs, which is the case for many Mg alloys. Nevertheless, some remaining ductility away from the necking region per sample should be possible to exploit by CBT. This work explores it with the emphasis on the RD direction as the least ductile. Figure 3b shows stress-strain curves based on the strain rate jump tests. The SRS constants calculated using the data are provided in Table 4. The alloy shows a moderate SRS along RD but small along TD. As a result, the applied crosshead velocity along with acceleration/deceleration can introduce small effects on the recorded load versus displacement along RD but negligible effects along TD.

Figure 4 shows a set of selected load versus displacement curves measured during CBT along RD for ZEK100 sheets. The curves in Fig. 4a are for variable bending depth

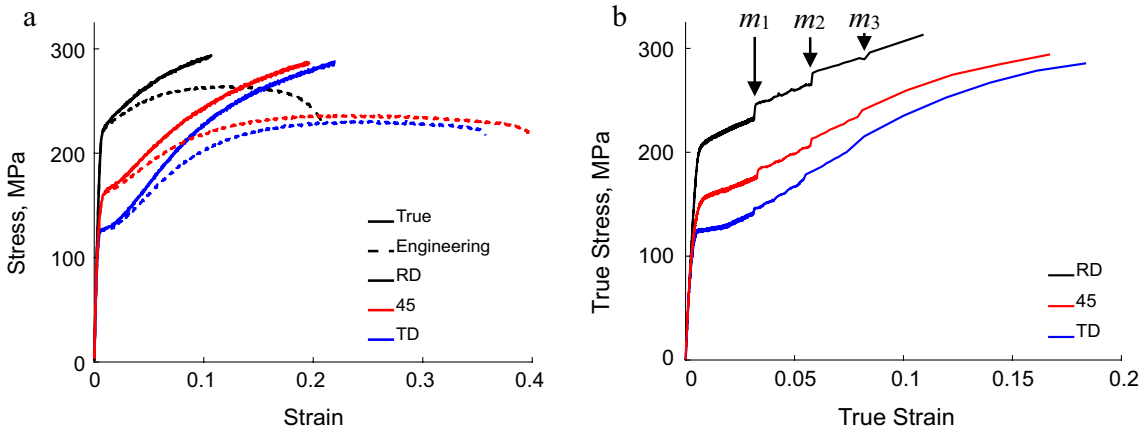

Fig. 3 **a** True (solid lines) and engineering (dashed line) stress-strain curves for as-received alloy ZEK100 sheets measured along RD, 45° direction, and TD in ST under a strain rate of 0.001/s at room temperature. **b** True stress-strain curves measured at room temperature under strain rate jumps from 0.0001/s to 0.001/s (m_1), from 0.001/s to 0.01/s (m_2), and from 0.01/s to 0.1/s (m_3) for the alloy along the three directions

Table 4 Strain rate sensitivity for alloy ZEK100-O

Direction	m_1	m_2	m_3	Mean
RD	0.0256	0.0202	0.0178	0.0212
45	0.0197	0.0153	0.0124	0.0158
TD	0.0086	0.0052	0.0094	0.0077

and those in Fig. 4b are for variable crosshead velocity. The load versus displacement curves recorded under ST are shown for reference. Evidently, the ETF is enhanced using CBT over the ST for any of the process parameters. Also, the axial forces are lower during CBT than those needed to sustain the plastic deformation in ST. The CBT curves show the characteristic quasi-periodic pattern of spikes and plateaus, while the ST curves exhibit the typical decreasing work hardening. The peaks in CBT occur when the rollers stop implying no bending i.e., the ST conditions. The patterns are in function of process parameters. The higher the bending determined with the bending depth and consequential bending strain/stress, the lower the required tensile strain/stress to deform the specimen for a given crosshead velocity. Increase in the bending depth increases the height/amplitude of the peaks, while the period in force is nearly constant for a fixed pull velocity. Increases in the crosshead velocity imply that the sheets are pulled faster during CBT meaning that the peaks are more spread i.e. the periods are wider and that the strain rate is also higher. The more spread peaks imply that the sheet is subjected to more tension since the bending deformation occurs only underneath the rollers. The figure shows that the crosshead velocity of 1.4 mm/s and the bending depth of 1.25 mm are optimal parameters for achieving the greatest ETF of ZEK100 along RD.

Figure 5 summarizes results of a comprehensive parametric study to optimize the process parameters. The optimization procedure consisted of varying pull speed and bend depth to maximize ETF. Constraints of the optimization consist of maximum bending depth and maximum pull speed possible to impose using the CBT machine. However, the relevant pull speeds and bend depts for the Mg sheet alloys are far below the machine capabilities. The machine can impose a bending depth of 5 mm along with a maximum pull speed of 33.5 mm/s. Three pull speeds and three bend depts are selected for the search of optimal parameters along the three sheet in-plane directions. The effect of more process parameters on ETF is presented in the Appendix 1 for completeness. The results imply that optimal bending depth is indeed 1.25 mm. The optimal bending conditions must not underbent or over-bent the sheet. In the former case, the sheet is under greater tension reducing ETF. In the latter case, bending stress/strain are high causing lower ETF. The optimal pull speed is indeed 1.4 mm/s for every test direction. Importantly the CBT has the greatest effect on the least ductile direction, which is the RD. As the CBT deformation inhibits the appearance of necking because ductility is depleted as uniformly as possible along the specimen, more of such ductility is possible to deplete along RD than 45° and TD. Nevertheless, moderate improvements in ETF are achieved even in 45° and TD. The available deformation in the sheet to deplete after exhausting the uniform elongation is small for these two directions likely because they are already ductile in ST. Specimens in CBT failed always perpendicular to the principal stress with no noticeable necking, while those in ST usually failed at an angle relative to the principal stress with small necking.

Grain structure of the ZEK100 alloy from the initial to deformed in CBT to 3 and 5 CBT cycles was characterized using EBSD in RD-ND plane. The inverse pole figure (IPF)

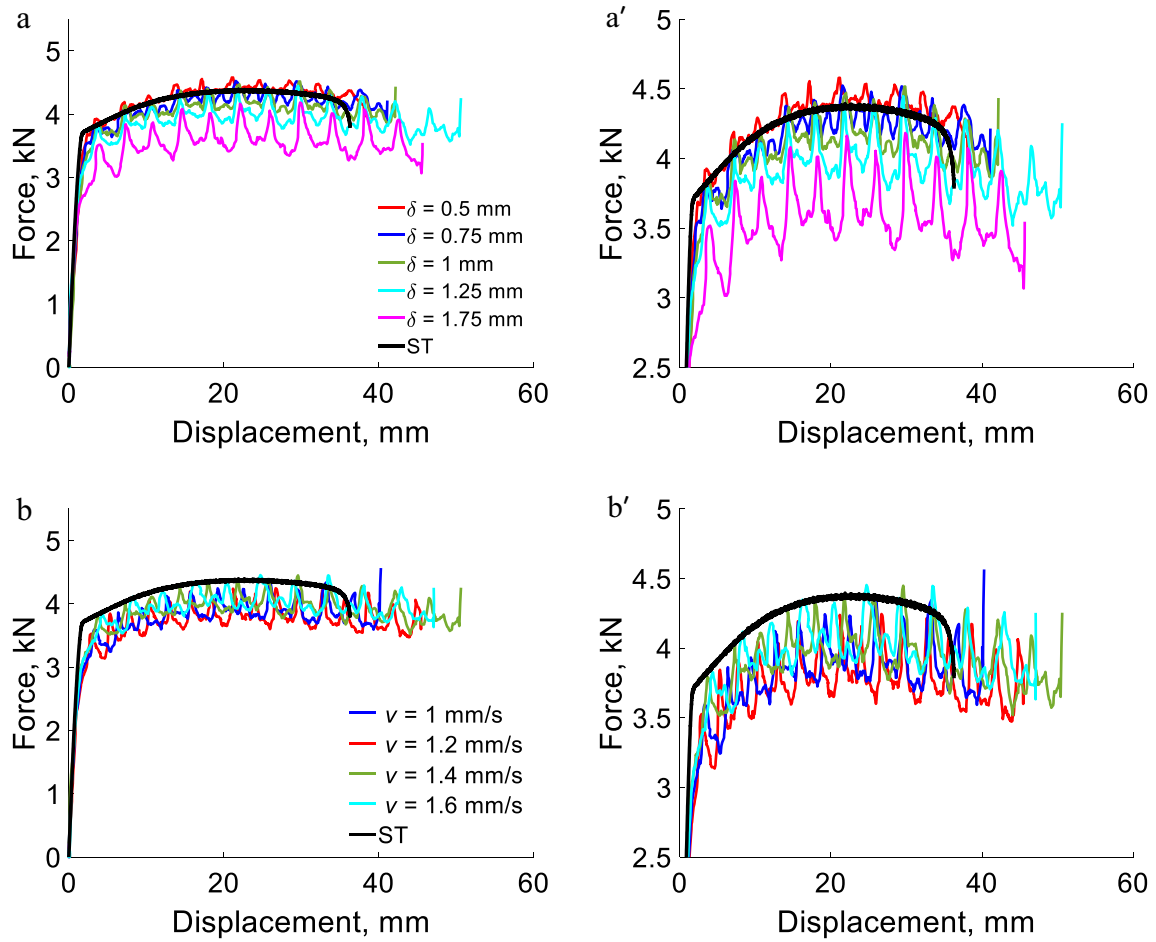

Fig. 4 Force-displacement curves measured during CBT testing of as-received ZEK100 sheets along RD under **a** fixed pull speed (v) of 1.4 mm/s and **b** fixed bend depth (δ) of 1.25 mm. The force-displacement curve in ST is shown in both (**a**) and (**b**) for reference. (**a'**) and (**b'**) are corresponding zoom ins to better observe the group of curves

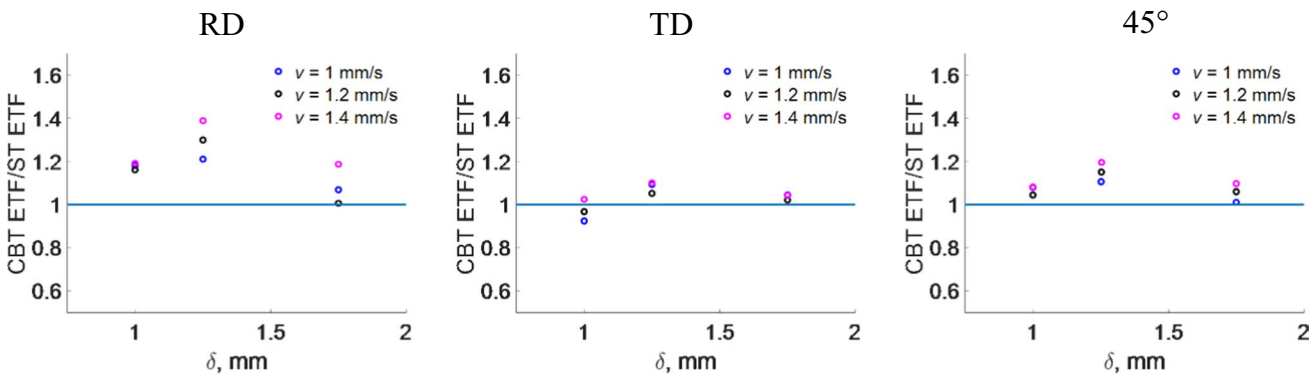

Fig. 5 ETF in CBT normalized by ETF in ST in versus bending depth for the three testing directions of alloy ZEK100

maps are shown in Fig. 6. The prominent red color in the maps indicates that that basal planes are predominantly contained or slightly tilted in the sheet plane i.e. the crystal **c**-axes of those grains is closely aligned with the ND axis of the sample. The initial average grain size in the alloy is 10 µm. Grains morphologically elongate and crystallographically reorient with plastic strain in CBT as a consequence of crystallographic slip with no evidence of deformation twinning.

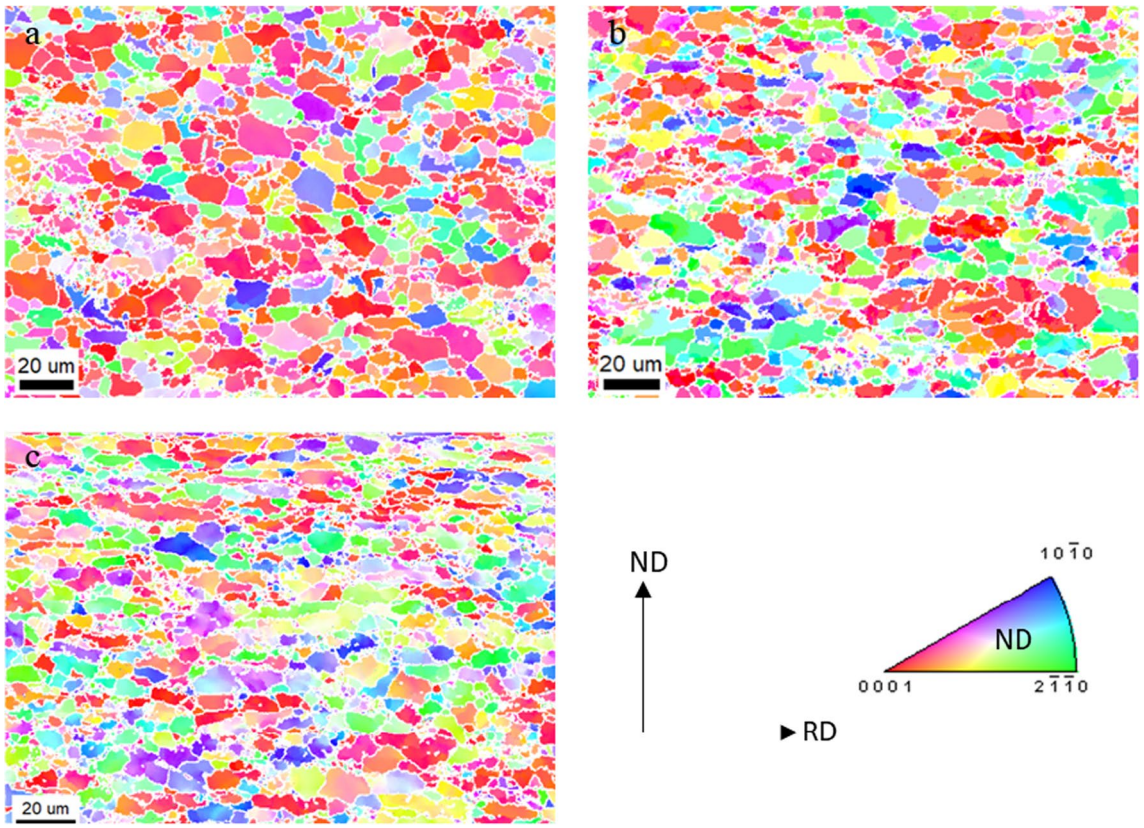

Fig. 6 IPF maps showing **a** an initial microstructure and two deformed microstructures in CBT along RD to **b** 3 CBT cycles and **c** 5 CBT cycles of alloy ZEK100. The colors in the maps correspond to the orientation of the ND sample axis with respect to crystal frames according to the IPF triangle. The scale-bars in the maps are 20 μm

Figure 7 shows the evolution of texture measured by neutron diffraction. The initial texture in the sheets is a moderately strong basal texture tilted in the TD. Texture evolution in ST is similar to texture evolution in CBT indicating similar stress/strain state in the sheets in ST and CBT. The intensities are slightly higher in CBT because of slightly higher strain levels achieved in CBT than in ST. As texture evolves with plastic strain more evolution takes place during deformation along 45° and TD in ST. Other than the formation of the prismatic $\left\{10\,\bar{1}\,0\right\}$ pole along RD no obvious texture change from the initial one occurs under tension along RD. Primary change in texture pertains to the basal pole with also some realignment in the prismatic poles under tension in the TD. The texture evolution in tension along the TD is distinct for that observed under tension along the RD. The measured pole figures in tension along TD reveal that grains reorient their **c**-axes from tilted parallel to the TD to lie tilted along the RD. Moreover, spreads of basal poles approximately 15° from the ND form. Realignment of the basal intensities is also noticeable under tension in 45° along the pull direction. Similar changes in texture under tension of ZEK100 were reported in [75] as well as in [76]. The changes in texture are gradual suggesting the slip dominated deformation. Prismatic and basal slip systems are expected to dominate the deformation, which is common for Mg alloy sheets pulled in tension in-plane. Since increasing fraction of grains are oriented such that their **c**-axis are compressed and the tensile twinning does not operate, the compressive strain along the **c**-axes must be accommodated by some pyramidal slip. Measured SRS of the alloy along with the initial texture reveal more activity of less SRS slip systems along TD than RD [77]. The measured values of SRS per slip mode are [78]: $m^{\alpha=1} = 1 \times 10^{-6}$ for basal slip systems, $m^{\alpha=2} = 2.35 \times 10^{-2}$ for prismatic slip systems, and $m^{\alpha=3} = 7.42 \times 10^{-3}$ for pyramidal slip systems [79]. More basal slip with less prismatic and pyramidal slip activity operates in tension along TD than along RD [75].

Figure 8 shows the stress-strain response of the alloy based on testing sub-size specimens of sheets treated by CBT to a certain uniform strain determined by the number of CBT cycles, a few of which were subsequently annealed at 100 °C, 200 °C, and 300 °C for recovery and partial recrystallization. The treatment by CBT was under 1.4 mm/s crosshead velocity and 1.25 bending depth. In making these specimens, the CBT tests were interrupted after a specified number of cycles was achieved and then a few specimens underwent annealing. The sub-size specimens were then cut out from the 3x region

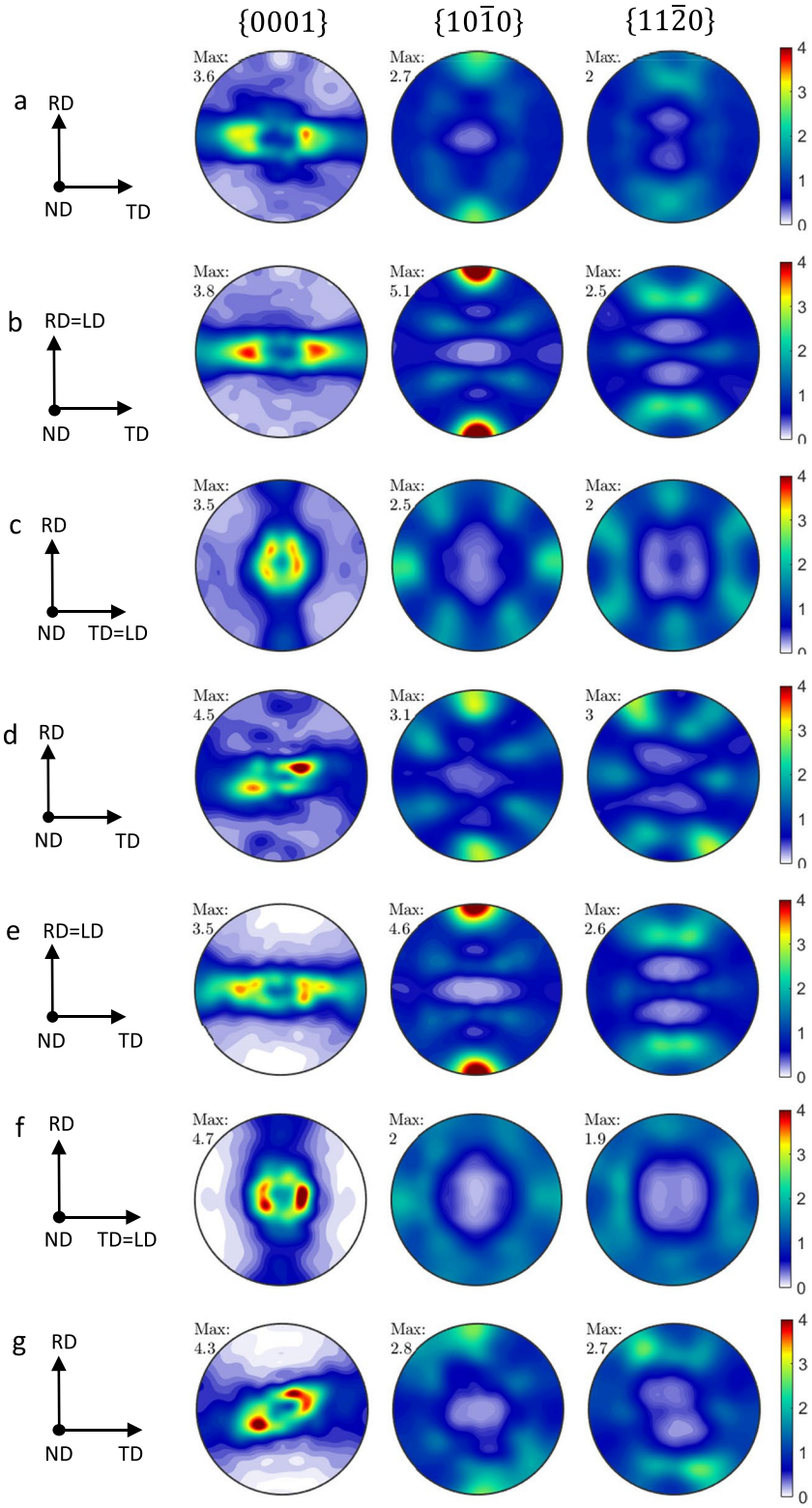

Fig. 7 Pole figures (stereographic) showing texture evolution in alloy ZEK100 from **a** an initial texture to deformed textures in CBT to fracture (under 1.25 mm bend depth and 1.4 mm/s crosshead velocity) along **b** RD, **c** TD, and **d** 45° and in ST to fracture along **e** RD, **f** TD, and **g** 45°

of the CBT specimens. The specimens were used to evaluate increases in strength and the amount of residual ductility in the alloy upon the treatments. The stress-strain curves for the as-received (initial) ZEK100 are shown to facilitate comparisons for every direction. The results show that the strength of the alloy can substantially increase over the as received material by treating it by CBT at the expanse of the residual elongation. The Appendix 1 presents the quantitative data extracted

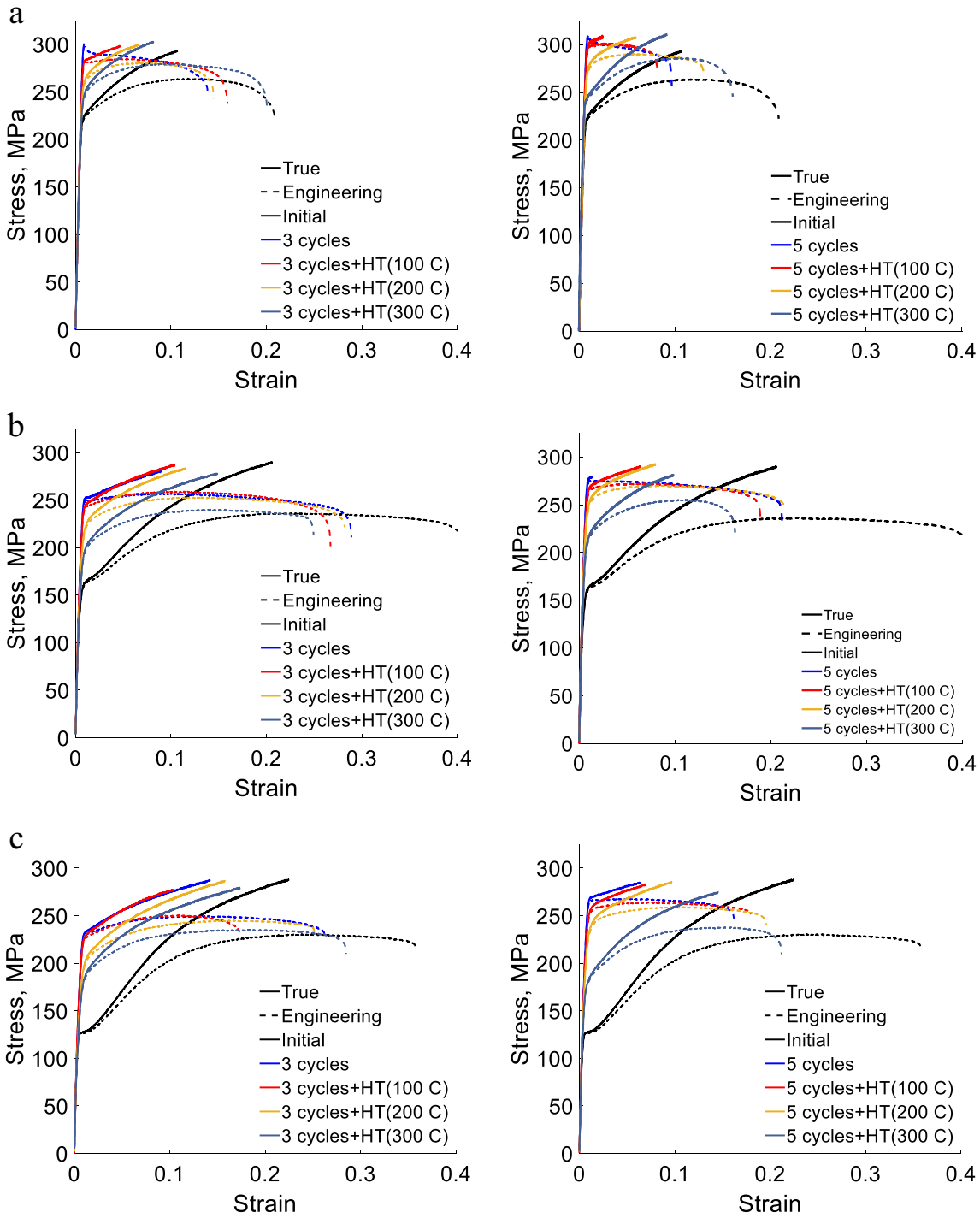

Fig. 8 True (solid lines) and engineering (dashed line) stress-strain curves measured at room temperature under a strain rate of 0.001/s using sub-sized specimens of the alloy ZEK100 processed by CBT (under 1.4 mm/s crosshead velocity and 1.25 mm bend depth) and processed by CBT under the same conditions and then heat treated (HT) as indicated in the legends along: **a** RD, **b** 45°, and **c** TD. The curves for the as-received ZEK100 are also shown for reference

from the curves. The significant improvements in strength originate from dislocations due to cold work. Given no appreciable grain refinement and no twinning in the structure after CBT, the strength increase must be owing to the increase in dislocation density. Cellular dislocation structures in Al alloys [51] and dislocation tangles in steels [52] were observed in these earlier CBT works. Strength of the alloy is found to increase by a factor of 1.4 along the RD and a factor of 2

along the TD. Interestingly, the alloy does not have the previous anisotropy after CBT given more rapid hardening along TD than RD and the underlying texture changes. The texture changes much more drastically in tension along TD than along RD strengthening the TD direction and therefore contributing to the reduced anisotropy. Since the strength improves more along the soft direction than along the hard direction, the alloy anisotropy reduces. Subsequent annealing can restore some ductility trading off the strength. Significantly, the strength can increase for about 40% along the soft direction, while reducing the anisotropy and preserving at least 10% of the alloy ductility in every direction.

Characterization of microstructural evolution using EBSD during annealing is shown in Fig. 9. The IPF maps show the extent of recovery and recrystallization. Only the treatment at 300 °C for 1 h induced partial recrystallization, while the treatments at 100 and 200 °C cause recovery of the alloy. The sheets after 1 h at 100 °C and 200 °C have similar grain structure like the sheet after 5 CBT cycles. Therefore, only different amounts of recovery operated with more at the higher temperature. Pole figures in Fig. 10 measured by neutron diffraction show the texture evolution during annealing and confirm recovery at 200 °C and partial recrystallization at 300 °C. The structure at 400 °C after 1 h would be fully annealed and the material would behave like the as received one.

Similar processing and testing of BioMg250 and Mg4Li sheet alloys produced even better results in terms of enhancing elongation and improving the contrasting strength and ductility properties. First, Fig. 11 shows the initial microstructures and corresponding textures in these alloys. The alloys exhibit fully recrystallized microstructures with average grain size of 13 µm for BioMg250 and 38 µm for Mg4Li. Texture in the BioMg250 alloy is moderately strong with basal peaks slightly spread in the TD. The MgLi alloy has a typical extrusion texture with a spread of **c**-axes perpendicular to the ED with two maxima tilted ~ 35° towards NED (or TD). As a result of such textures TD for the BioMg250 alloy and NED for the Mg4Li alloy should be softer directions with more basal slip activity. Figure 12 shows stress-strain curves measured for these two alloys. Interestingly, the alloy BioMg250 shows similar trend in anisotropy as the alloy ZEK100 but less pronounced, likely owing to texture. As expected, the alloy Mg4Li is mush softer than the two other alloys. SRS of BioMg250 and

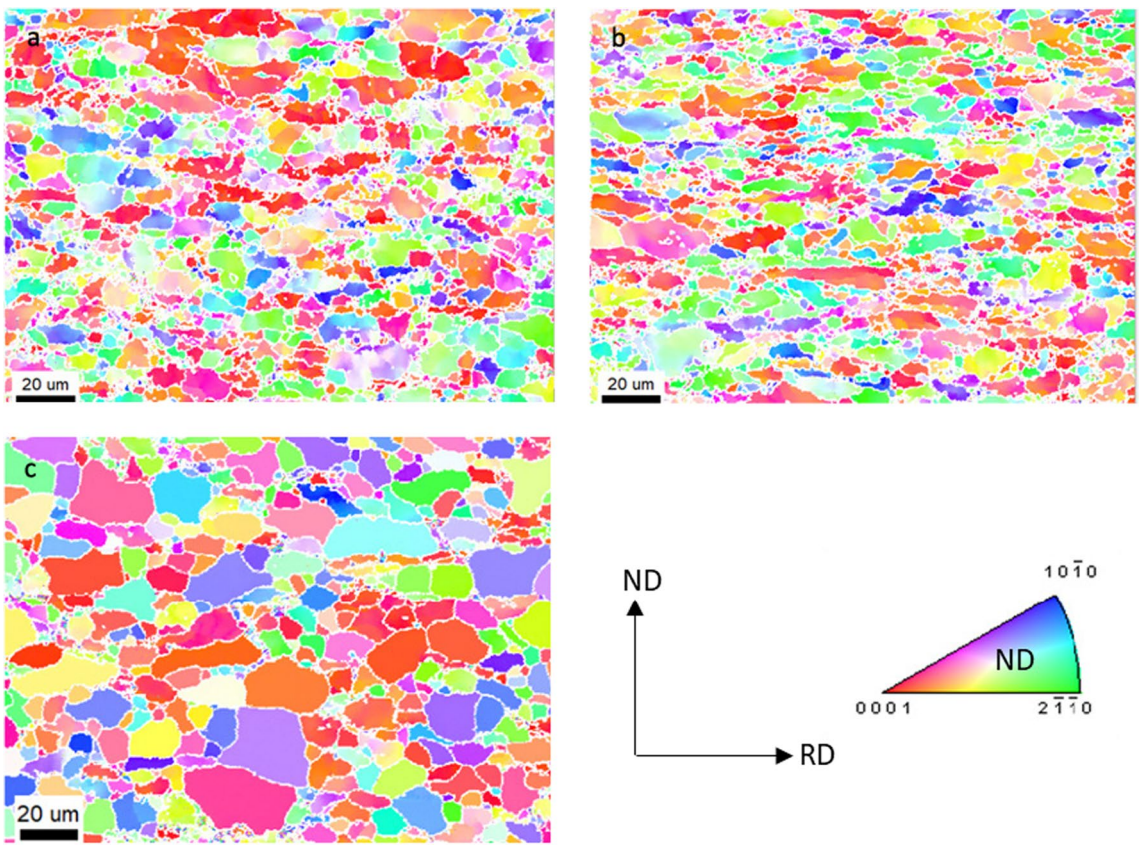

Fig. 9 IPF maps showing microstructures of alloy ZEK100 after 5 CBT cycles along RD followed by annealing at **a** 100 °C mm for 1 h, **b** 200 °C mm for 1 h, and **d** 300 °C for 1 h. The colors in the maps correspond to the orientation of the ND sample axis with respect to crystal frames according to the IPF triangle. The scale-bars in the maps are 20 µm

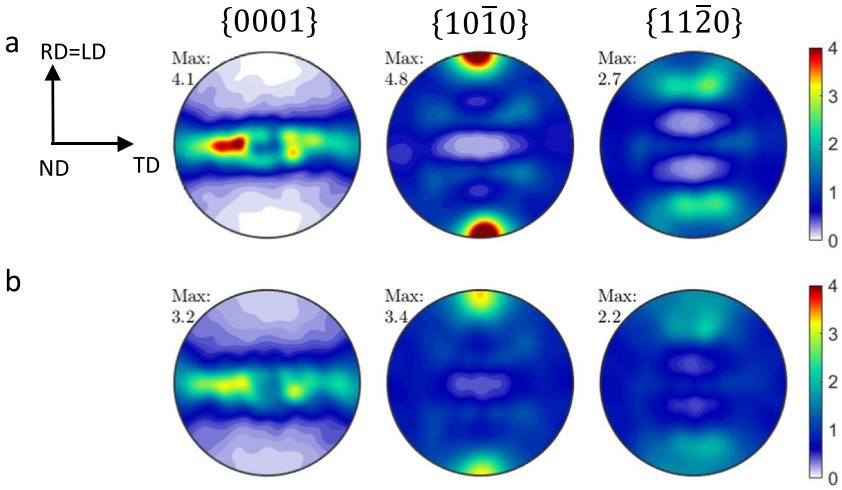

Fig. 10 Pole figures (stereographic) showing texture evolution of alloy ZEK100 deformed in CBT along RD to 5 cycles (under 1.25 mm bend depth and 1.4 mm/s crosshead velocity) and then annealed at **a** 200 °C for 1 h and **b** 300 °C for 1 h

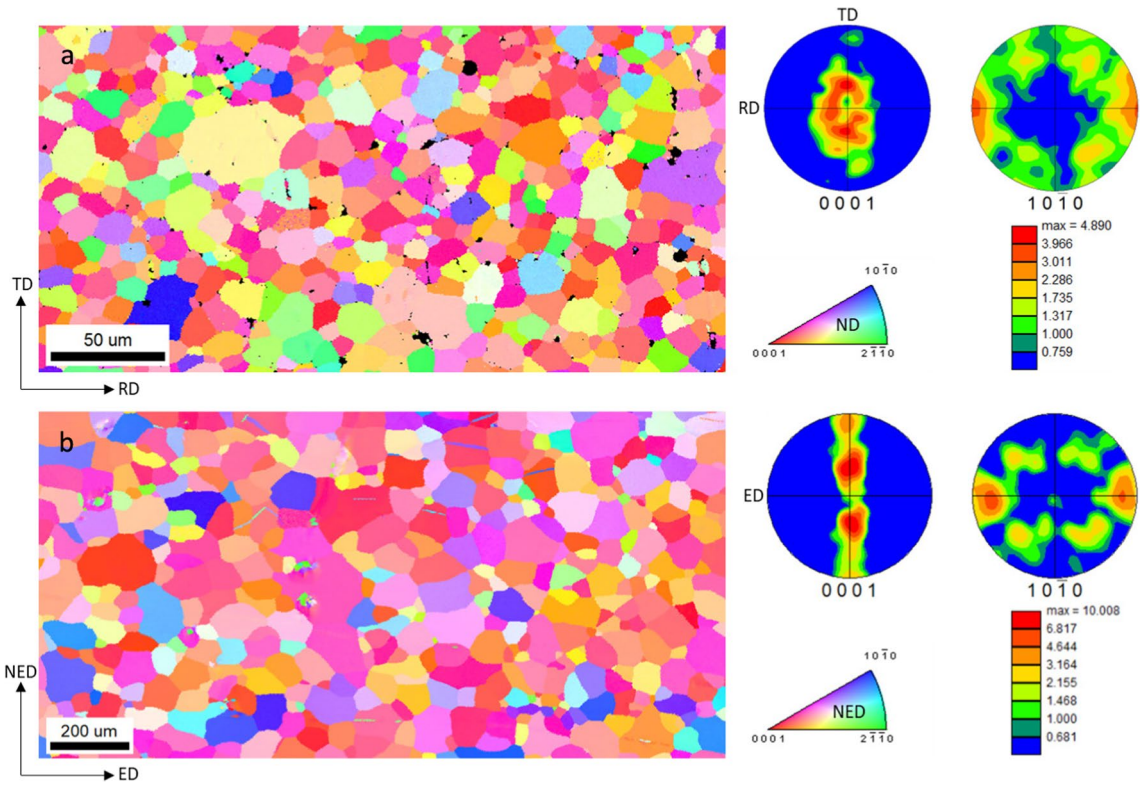

Fig. 11 IPF maps and pole figures showing the initial microstructures and textures of **a** BioMg250 and **b** Mg4Li alloys. The colors in the maps correspond to the orientation of the selected sample axes indicated in the IPF triangle per map with respect to crystal frames according to the IPF triangle

Mg4Li sheet alloys was also measured. Table 5 shows the results indicating small SRS, especially for the Mg4Li alloy.

Figure 13 shows load versus displacement curves for the alloys tested in CBT. The results confirm that 1.25 bending depts continues to be optimal. The improvements in elongation are slightly greater than obtained for alloy ZEK100, especially for the Mg4Li alloy. The uniform pre-straining possible to achieve to large strain in CBT can improve strength of these two alloys more than two times. The pre-straining was performed under the optimized process parameters. The subsequent annealing can induce favorable tradeoffs in strength versus ductility, as Fig. 14 displays. Quantitative data for properties from the curves is provided in the Appendix 1.

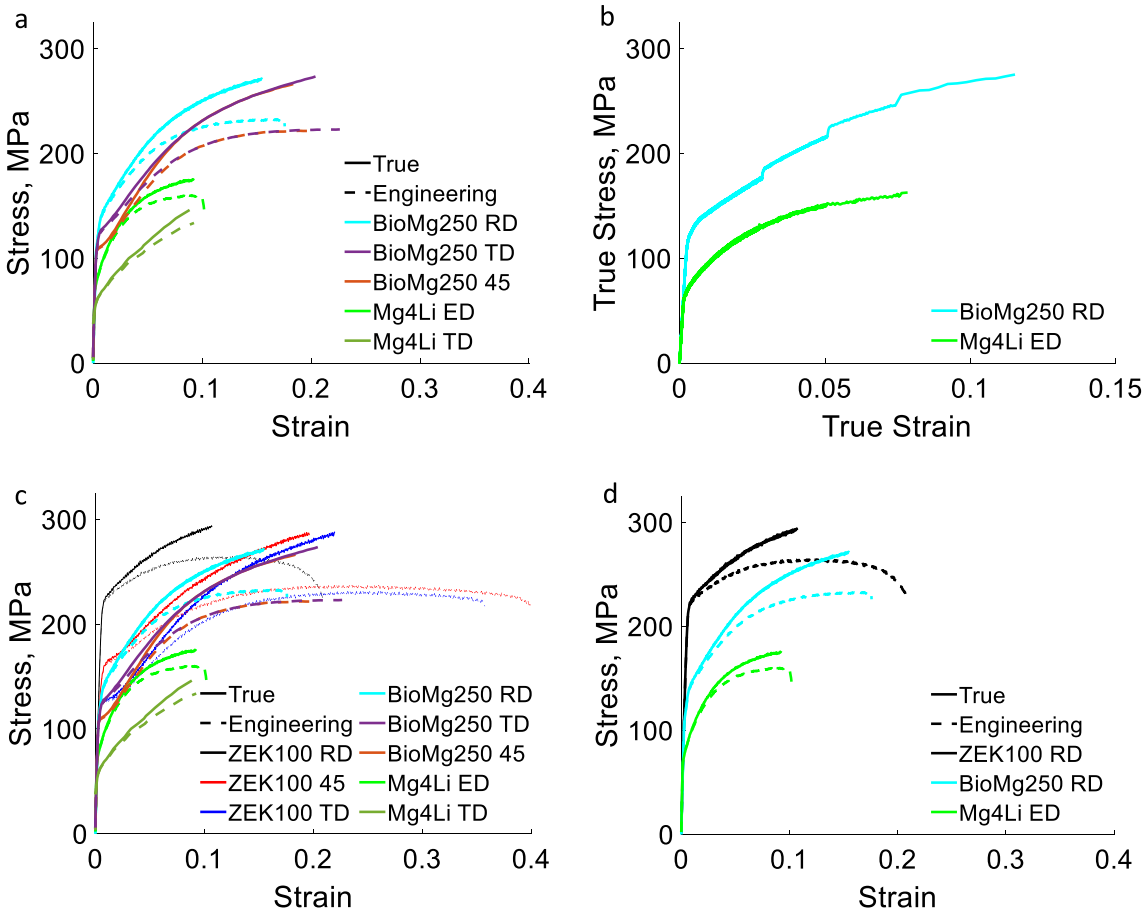

Fig. 12 **a** True (solid lines) and engineering (dashed line) stress-strain curves for as-received alloys: BioMg250 along RD, 45°, and TD and Mg4Li along the extruded direction (ED) and transverse direction (TD) measured in ST under a strain rate of 0.001/s at room temperature. **b** True stress-strain curves measured at room temperature under strain rate jumps from 0.0001/s to 0.001/s (m_1), from 0.001/s to 0.01/s (m_2), and from 0.01/s to 0.1/s (m_3) for: BioMg250 along RD and Mg4Li along ED. **c**, **d** Plots of the data provided to facilitate comparisons

Table 5 Strain rate sensitivities of alloys BioMg250 and Mg4Li

Direction	m_1	m_2	m_3	Mean
BioMg250	0.0206	0.0173	0.0218	0.0199
Mg4Li	0.0064	0.0036	0.0049	0.005

Discussion

This work examined the behavior of three Mg sheet alloys in CBT. Like most of Mg alloys, these alloys exhibit a relatively large strain hardening rates and small necking. The

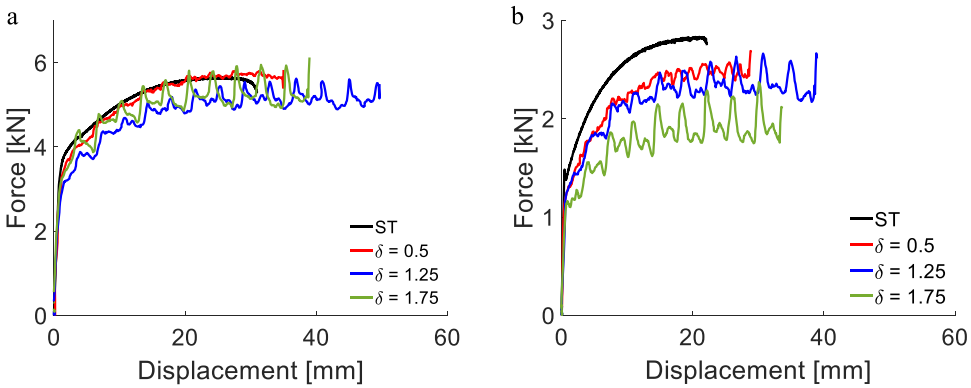

Fig. 13 Force-displacement curves measured during CBT testing of **a** BioMg250 along RD and **b** Mg4Li along ED under fixed pull speed (v) of 1.4 mm/s and variable bend depth (δ) as specified in the legends. The force-displacement curves measured in ST are shown for reference

work showed that CBT can have positive influence on the ETF and axial load levels, especially under the optimized process parameters. Particularly, under a normalized bending depth of 1.25 and a crosshead velocity of 1.4 mm/s, ETF of all alloys can improve for at least 40%. Figure 15 shows the maximum improvements achieved per alloy. The improved ETF implies improved formability. Given the relatively low value of the optimal bend depth established for the alloys, the bending stress/strain imposed by CBT was rather small. Greater bending caused the sheets to fail much sooner. These outcomes are in contrast to studies on other materials like aluminum alloys and dual-phase steels, which allowed more bending by CBT [80].

The hardening was evenly depleted in ST up until necking and in CBT to greater strain levels than those achievable in ST. The necking instability set sooner in ST then in CBT under the optimized process parameters. The three alloys, like most of Mg alloys, fail rapidly after forming an instability and necking in ST. After the necking localization, the neck accumulates some more plastic strain beyond the uniform, while the rest of the specimen unloads with some remaining capacity to deform. In CBT, the gauge section elongates incrementally underneath the rollers without appreciable necking. The CBT process deforms the sheet uniformly while exploiting ductility of the entire gauge section to a larger extent than the onset of necking in ST. However, in Mg alloys, such remaining ductility is not large but only moderate such that the improvements in ETF by CBT are not as large as those for aluminum alloys and steels.

Superposition of bending tension over the tensile load dropped the force required to cause the plastic flow of the alloys. As a result, the force versus displacement curves in CBT are lower than those in ST meaning that the CBT processing is carried out at an axial stress level below the yield stress of the specimen. The greatest stress is the outer surface of the sheet undergoing CBT. The magnitude

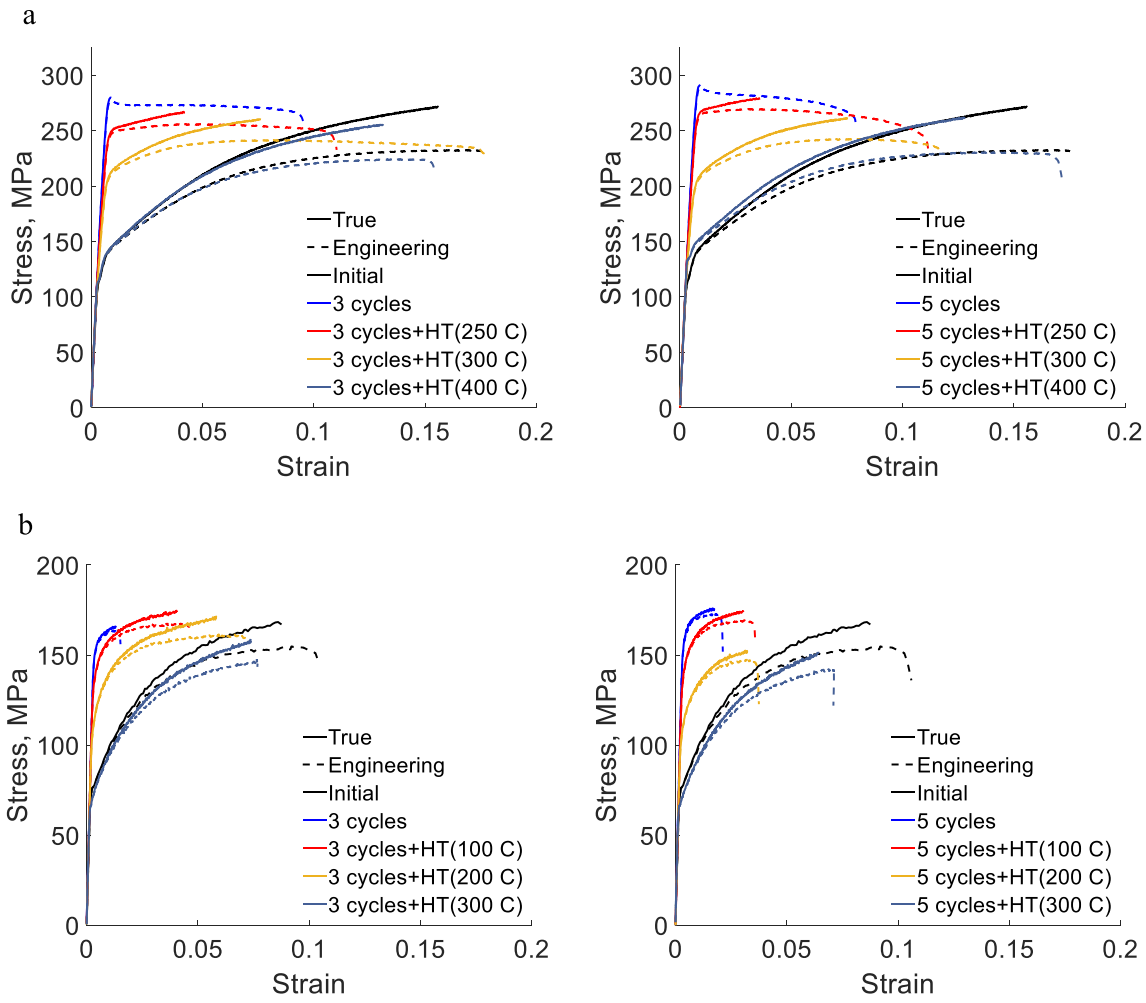

Fig. 14 True (solid lines) and engineering (dashed line) stress-strain curves measured at room temperature under a strain rate of 0.001/s using sub-sized specimens of **a** BioMg250 along RD and **b** Mg4Li along ED processed by CBT (under 1.4 mm/s crosshead velocity and 1.25 mm bend depth) and processed by CBT under the same conditions and then heat treated (HT) as indicated in the legends. The curves for the as-received alloys are also shown for reference

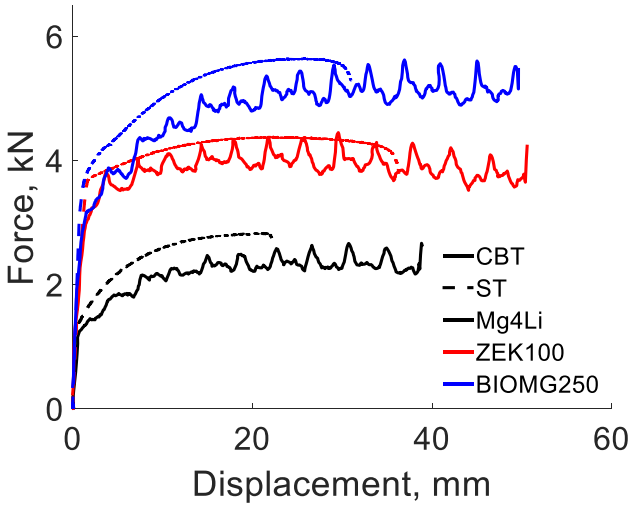

Fig. 15 The force-displacement curves summarizing the maximum improvements in the elongation achieved by CBT for the three Mg sheet alloys: ZEK100 along RD (Fig. 3), BioMg250 along RD (Fig. 13a), and Mg4Li along ED (Fig. 13b)

of stress is a function of sheet thickness. Moreover, the combined bending and tension induce a non-symmetric tension/compression stress/strain profile with the neutral axis cyclically shifting to sheet surfaces opposite of the roller over which the sheet is going over. Thinner sheets can have the neutral axis leave the sheet thickness causing the entire sheet to be in tension. If this happens, the stabilizing mechanisms, which is the compressive portion of the stress/strain profile vanishes causing the sheet to fail sooner. Hence, the thicker sheets can benefit more from CBT than thinner sheets. Part of the reason, BioMg250 and Mg4Li alloys benefiting more from CBT than ZEK100 can be attributed to their thicknesses.

The work showed that strength of the alloys can be substantially increased by CBT and moreover the strength and residual ductility can be treaded off by CBT and annealing. The enhancements in strength were mainly attributed to the increase in density of dislocations formed during CBT, while some hardening effects due to precipitation hardening could not be ruled out, especially at the highest annealing temperatures [81]. As expected, the deformation of the alloys was slip dominated. The characterization of texture evolution for ZEK100 revealed expected texture evolution under tension with slightly higher intensities under CBT than ST. Finally, the measured SRS for the alloys was consistent with the literature of Mg alloys [82]. The deformation under tension was expected to be dominated by prismatic slip, along with some basal slip to a smaller extent, and some minor contribution of pyramidal slip [82–85]. Given that these slip modes exhibit different SRS, the relative amounts of deformation modes accommodating the plasticity in tension and measured SRS in this work verify the overall SRSs.

Conclusions

This work employed CBT and annealing to enhance elongation and establish tradeoffs in strength and ductility of several Mg sheet alloys: ZEK100, BioMg250, and Mg4Li. The CBT process parameters consisting of the bending depth and crosshead velocity were varied to maximize achievable ETF for the sheets of the alloys. The greatest ETF was achieved under 1.4 mm/s crosshead velocity and 1.25 bending depth yielding over 40% improvement in EFT using CBT over ST for every alloy. The work further showed that the uniform elongation using CBT can provide a promising means to improve the tradeoff between strength and ductility by applying CBT to a certain number of cycles and then annealing. Finally, EBSD and neutron diffraction microstructure characterization techniques were employed to measure the initial microstructure and texture and microstructural evolution of the alloys with plastic strain. Comprehensive data sets and analyses for the three alloys allowed us to draw several conclusions:

- A small capacity to deform upon necking in ST characteristic of Mg alloys facilitated a small amount of ductility to be deplete throughout the sheet. Nevertheless, at least 40% improvements in ETF were achieved using CBT for every alloy by postponing the onset of necking instability. Slightly better results for BioMg250, and Mg4Li alloys were attributed in part to these sheet thicknesses. In general, thicker sheets contain the neutral axis inside their thickness increasing the stabilizing compressive segment of the stress/strain profile present in the sheet owing to bending.
- Strength of the alloys substantially increased by CBT processing, in some cases more than two times. Subsequent annealing of the alloy sheets could restore a great deal of their ductility and integrity to further deform. Significantly, the combination of CBT and annealing could increase strength of anisotropic alloys along the soft direction to decrease the anisotropy while preserving at least 10% of the alloy ductility in every direction. Driven by anisotropic hardening and microstructural evolution during CBT, the strength increased by a factor of 1.4 along the sheet strongest direction and a factor of 2 along the sheet softest direction for the alloy ZEK100.
- Characterization of microstructural evolution using EBSD and texture evolution using neutron diffraction revealed slip dominated deformation of the alloy ZEK100. Texture in CBT and ST evolved similarly revealing that the state of strains in the sheets was also similar with only levels of strain slightly greater in CBT than in ST. Since no twinning and appreciable grain refinement were observed in IPF maps of the deformed structures, the increase in strength was attributed to the increase in stored dislocations.

Appendix 1

This appendix presents a photograph of the CBT apparatus (Fig. 16) and tables with the elastic slope (E, GPa), yield strength (YS, MPa), ultimate tensile strength (UTS, MPa), strain at fracture, and uniform ductility inferred from the measured flow curves (Tables 6, 7, and 8). More data about ETF in CBT normalized by ETF in ST for the RD testing directions of alloy ZEK100 is presented in Fig. 17.

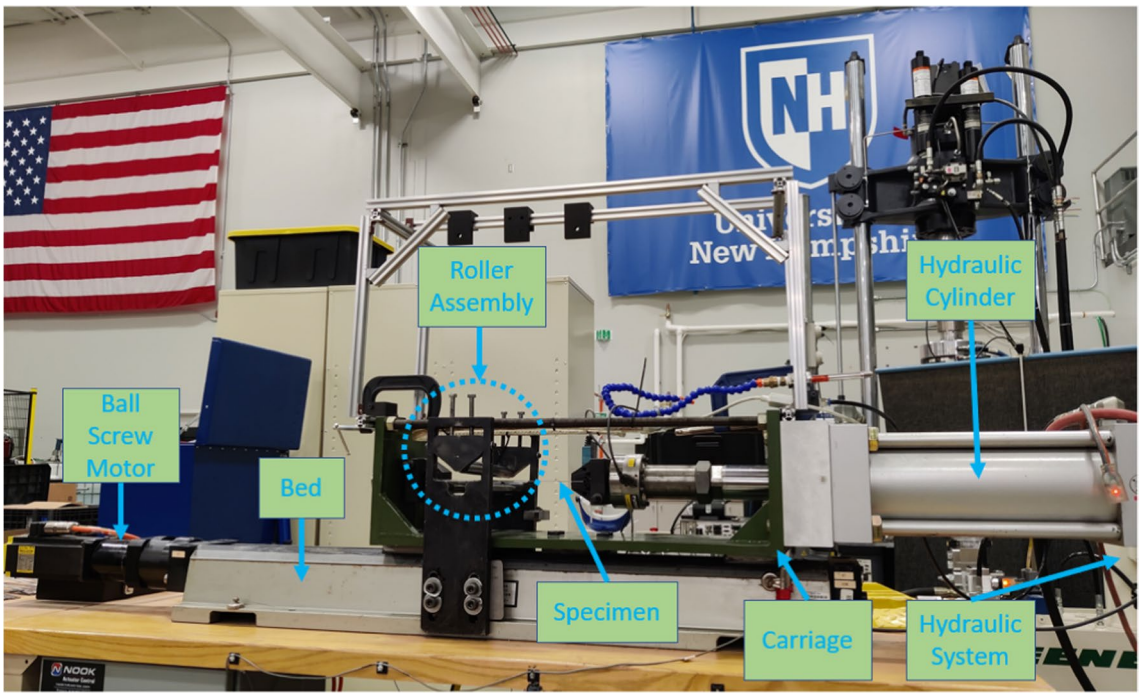

Fig. 16 A photograph of the apparatus for CBT highlighting the main components

Table 6 Mechanical properties from the flow curves for ZEK100

Name	Direction	E, GPa	YS, MPa (0.2% offset)	UTS, MPa	Strain At UTS	Strain At Fracture
As Received	RD	44.65	215	264	0.1196	0.2089
After 3 CBT cycles	RD	43.48	297	298	0.0072	0.1387
After 3 CBT cycles + HT (100 C)	RD	43.72	276	285	0.0462	0.1593
After 3 CBT cycles + HT (200 C)	RD	44.62	249	281	0.0668	0.1445
After 3 CBT cycles + HT (300 C)	RD	43.78	235	279	0.1023	0.2011
After 5 CBT cycles	RD	44.19	305	306	0.0079	0.0971
After 5 CBT cycles + HT (100 C)	RD	44.28	291	301	0.0235	0.0827
After 5 CBT cycles + HT (200 C)	RD	44.66	261	290	0.0594	0.1312
After 5 CBT cycles + HT (300 C)	RD	46.78	231	261	0.0969	0.161
As Received	45	46.7	137	236	0.2246	0.4054
After 3 CBT cycles	45	43.97	231	257	0.0919	0.2891
After 3 CBT cycles + HT (100 C)	45	44.56	219	259	0.1056	0.2674
After 3 CBT cycles + HT (200 C)	45	43.57	188	253	0.1285	0.2822
After 3 CBT cycles + HT (300 C)	45	42.33	166	240	0.1385	0.2495
After 5 CBT cycles	45	43.8	261	275	0.0106	0.212
After 5 CBT cycles + HT (100 C)	45	43.24	244	272	0.0638	0.1895
After 5 CBT cycles + HT (200 C)	45	44.94	221	270	0.0844	0.215

Table 6 (continued

Name	Direction	E, GPa	YS, MPa (0.2% offset)	UTS, MPa	Strain At UTS	Strain At Fracture
After 5 CBT cycles + HT (300 C)	45	44.84	192	255	0.1095	0.1632
As Received	TD	45.72	122	230	0.2502	0.3579
After 3 CBT cycles	TD	41.23	198	249	0.1307	0.2627
After 3 CBT cycles + HT (100 C)	TD	44.77	187	250	0.1074	0.1733
After 3 CBT cycles + HT (200 C)	TD	42.73	150	245	0.1673	0.2518
After 3 CBT cycles + HT (300 C)	TD	40.73	142	235	0.182	0.2852
After 5 CBT cycles	TD	42.76	240	268	0.0522	0.1621
After 5 CBT cycles + HT (100 C)	TD	43.31	219	264	0.07	0.1798
After 5 CBT cycles + HT (200 C)	TD	44.38	193	259	0.0932	0.1962
After 5 CBT cycles + HT (300 C)	TD	42.49	164	237	0.15	0.2119

Table 7 Mechanical properties from the flow curves for BioMg250

Name	Direction	E, GPa	YS, MPa (0.2% offset)	UTS, MPa	Strain At UTS	Strain At Fracture
As Received	RD	42.16	125	232	0.1664	0.1758
After 3 CBT cycles	RD	43.7	275	277	0.0071	0.0961
After 3 CBT cycles + HT (250 C)	RD	44.91	234	256	0.042	0.1106
After 3 CBT cycles + HT (300 C)	RD	44.27	194	241	0.0769	0.1769
After 3 CBT cycles + HT (400 C)	RD	44.23	126	224	0.1383	0.1541
After 5 CBT cycles	RD	43.36	287	289	0.0072	0.0791
After 5 CBT cycles + HT (250 C)	RD	44.95	259	269	0.0267	0.112
After 5 CBT cycles + HT (300 C)	RD	43.65	195	242	0.0789	0.119
After 5 CBT cycles + HT (400 C)	RD	44.65	140	230	0.1386	0.172

Table 8 Mechanical properties from the flow curves for Mg4Li

Name	Direction	E, GPa	YS, MPa (0.2% offset)	UTS, MPa	Strain At UTS	Strain At Fracture
As Received	ED	42.78	75	155	0.0901	0.111
After 3 CBT cycles	ED	49.09	158	164	0.0113	0.0149
After 3 CBT cycles + HT (100 C)	ED	47.78	145	167	0.0338	0.0481
After 3 CBT cycles + HT (200 C)	ED	48.74	120	162	0.058	0.0731
After 3 CBT cycles + HT (300 C)	ED	48.99	75	147	0.0745	0.0758
After 5 CBT cycles	ED	51.17	162	173	0.0156	0.0207
After 5 CBT cycles + HT (100 C)	ED	47.25	149	169	0.0291	0.0354
After 5 CBT cycles + HT (200 C)	ED	48.94	116	147	0.0308	0.0367
After 5 CBT cycles + HT (300 C)	ED	49.87	72	142	0.0647	0.0711

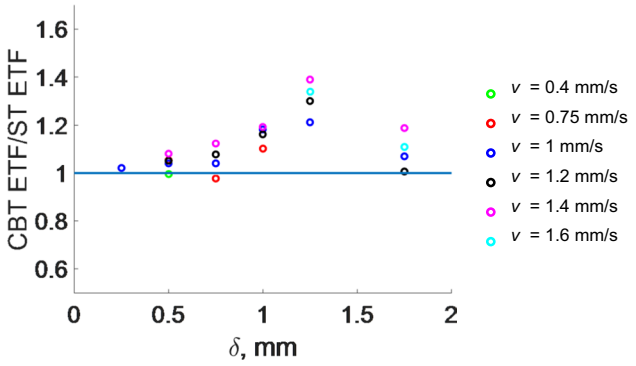

Fig. 17 ETF in CBT normalized by ETF in ST for the RD testing directions of alloy ZEK100

Acknowledgements This work is based upon projects supported by the U.S. National Science Foundation under a CAREER grant CMMI-1650641 and a GOALI grant CMMI-2147122. Rolled sheets of ZEK100 were provided by Michael Worswick of University of Waterloo. Rolled sheets of BioMg250 were provided by nanoMAG, LLC. Extruded sheets of Mg4Li were provided by Technische Universität Berlin. These are gratefully acknowledged.

Data availability The raw/processed data required to reproduce these findings cannot be shared at this time due to technical or time limitations.

Declarations

Conflict of interest The authors declare that they have no conflict of interest.

References

1. Cho K, Sano T, Doherty K, Yen C, Gazonas G, Montgomery J, Moy P, Davis B, DeLorme R (2009) Magnesium technology and manufacturing for ultra lightweight armored ground vehicles DTIC Document. https://apps.dtic.mil/sti/citations/ADA499411
2. Mordike BL, Ebert T (2001) Magnesium: Properties - applications - potential. Mater Sci Eng A 302:37–45
3. Vasilev E, Popov D, Somayazulu M, Velisavljevic N, Knezevic M (2023) White Laue and powder diffraction studies to reveal mechanisms of HCP-to-BCC phase transformation in single crystals of mg under high pressure. Sci Rep 13:2173
4. (2008) Magnesium's tough strength endures abuse to protect portable electronic devices. Int Magnesium Assoc. https://doczz.net/doc/6470274/magnesium%E2%80%99s-tough-strength-endures-abuse-to-protect-porta...
5. Dziuba D, Meyer-Lindenberg A, Seitz JM, Waizy H, Angrisani N, Reifenrath J (2013) Long-term in vivo degradation behaviour and biocompatibility of the magnesium alloy ZEK100 for use as a biodegradable bone implant. Acta Biomater 9:8548–8560
6. Alam ME, Pal S, Decker R, Ferreri NC, Knezevic M, Beyerlein IJ (2020) Rare-earth- and aluminum-free, high strength dilute magnesium alloy for Biomedical Applications. Sci Rep 10:15839
7. Wonsiewicz BC, Backofen WA (1967) Plasticity of magnesium crystals. Trans Metall Soc AIME 239:1–57
8. Savage DJ, Beyerlein IJ, Mara NA, Vogel SC, McCabe RJ, Knezevic M (2020) Microstructure and texture evolution in Mg/Nb layered materials made by accumulative roll bonding. Int J Plast 125:1–26
9. Vasilev E, Wang J, Knezevic M (2022) A structure metric for quantitative assessment of fracture surfaces in 3D conceived based on confocal laser scanning microscopy data. Mater Charact 194:112369
10. Vasilev E, Knezevic M (2023) Experimental characterization of voids and surrounding microstructures developed under tension of Mg, Mg–3Zn, and Ti: A statistical study. Mater Sci Eng A 862:144411
11. Knezevic M, Levinson A, Harris R, Mishra RK, Doherty RD, Kalidindi SR (2010) Deformation twinning in AZ31: influence on strain hardening and texture evolution. Acta Mater 58:6230–6242
12. Zecevic M, Beyerlein IJ, Knezevic M (2018) Activity of pyramidal I and II < c + a > slip in mg alloys as revealed by texture development. J Mech Phys Solids 111:290–307
13. Nugmanov D, Knezevic M, Zecevic M, Sitdikov O, Markushev M, Beyerlein IJ (2018) Origin of plastic anisotropy in (ultra)-fine-grained Mg–Zn–Zr alloy processed by isothermal multi-step forging and rolling: experiments and modeling. Mater Sci Eng A 713:81–93
14. Wu X, Proust G, Knezevic M, Kalidindi SR (2007) Elastic-plastic property closures for hexagonal close-packed polycrystalline metals using first-order bounding theories. Acta Mater 55:2729–2737
15. Tam KJ, Vaughan MW, Shen L, Knezevic M, Karaman I, Proust G (2020) Modelling the temperature and texture effects on the deformation mechanisms of magnesium alloy AZ31. Int J Mech Sci 182:105727
16. Tam KJ, Vaughan MW, Shen L, Knezevic M, Karaman I, Proust G (2021) Modelling dynamic recrystallisation in magnesium alloy AZ31. Int J Plast 142:102995
17. Zecevic M, Knezevic M, McWilliams B, Lebensohn RA (2020) Modeling of the thermo-mechanical response and texture evolution of WE43 mg alloy in the dynamic recrystallization regime using a viscoplastic self-consistent formulation. Int J Plast 130:102705
18. Zecevic M, Lebensohn RA, McCabe RJ, Knezevic M (2019) Modelling recrystallization textures driven by intragranular fluctuations implemented in the viscoplastic self-consistent formulation. Acta Mater 164:530–546
19. Hirsch J, Al-Samman T (2013) Superior light metals by texture engineering: optimized aluminum and magnesium alloys for automotive applications. Acta Mater 61:818–843
20. Knezevic M, Crapps J, Beyerlein IJ, Coughlin DR, Clarke KD, McCabe RJ (2016) Anisotropic modeling of structural components using embedded crystal plasticity constructive laws within finite elements. Int J Mech Sci 105:227–238
21. Knezevic M, Kalidindi SR, Mishra RK (2008) Delineation of first-order closures for plastic properties requiring explicit consideration of strain hardening and crystallographic texture evolution. Int J Plast 24:327–342
22. Knezevic M, Lebensohn RA, Cazacu O, Revil-Baudard B, Proust G, Vogel SC, Nixon ME (2013) Modeling bending of α-titanium with embedded polycrystal plasticity in implicit finite elements. Mater Sci Eng A 564:116–126
23. Jahedi M, Paydar MH, Zheng S, Beyerlein IJ, Knezevic M (2014) Texture evolution and enhanced grain refinement under high-pressure-double-torsion. Mater Sci Eng A 611:29–36
24. Imandoust A, Barrett CD, Al-Samman T, Inal KA, El Kadiri H (2017) A review on the effect of rare-earth elements on texture evolution during processing of magnesium alloys. J Mater Sci 52:1–29
25. Vasilev E, Wang J, Zhu G, Knezevic M (2023) Influence of deformation banding instabilities on small scale yielding of a

Mg–Nd alloy revealed by in-situ digital image correlation. Sci Rep 13:5767
26. Wang J, Zhu G, Wang L, Vasilev E, Park J-S, Sha G, Zeng X, Knezevic M (2021) Origins of high ductility exhibited by an extruded magnesium alloy Mg-1.8Zn-0.2Ca: experiments and crystal plasticity modeling. J Mater Sci Technol 84:27–42
27. Jahedi M, McWilliams BA, Kellogg FR, Beyerlein IJ, Knezevic M (2018) Rate and temperature dependent deformation behavior of as-cast WE43 magnesium-rare earth alloy manufactured by direct-chill casting. Mater Sci Eng A 712:50–64
28. Jahedi M, McWilliams BA, Knezevic M (2018) Deformation and fracture mechanisms in WE43 magnesium-rare earth alloy fabricated by direct-chill casting and rolling. Mater Sci Eng A 726:194–207
29. Jahedi M, McWilliams BA, Moy P, Knezevic M (2017) Deformation twinning in rolled WE43-T5 rare earth magnesium alloy: influence on strain hardening and texture evolution. Acta Mater 131:221–232
30. Li Q, Ye W, Gao H, Gao L (2019) Improving the corrosion resistance of ZEK100 magnesium alloy by combining high-pressure torsion technology with hydroxyapatite coating. Mater Des 181:107933
31. Ghorbanpour S, McWilliams BA, Knezevic M (2019) Effect of hot working and aging heat treatments on monotonic, cyclic, and fatigue behavior of WE43 magnesium alloy. Mater Sci Eng A 747:27–41
32. Ghorbanpour S, McWilliams BA, Knezevic M (2019) Low-cycle fatigue behavior of rolled WE43-T5 magnesium alloy. Fatigue Fract Eng Mater Struct 42:1357–1372
33. Savage DJ, McWilliams BA, Vogel SC, Trujillo CP, Beyerlein IJ, Knezevic M (2020) Mechanical behavior and texture evolution of WE43 magnesium-rare earth alloy in Split-Hopkinson pressure bar and Taylor impact cylinder testing. Int J Impact Eng 143:103589
34. Zecevic M, Roemer T, Knezevic M, Korkolis Y, Kinsey B (2016) Residual ductility and microstructural evolution in continuous-bending-under-tension of AA-6022-T4. Materials 9:130
35. Emmens WC, Sebastiani G, van den Boogaard AH (2010) The technology of incremental sheet Forming—A brief review of the history. J Mater Process Technol 210:981–997
36. Music O, Allwood J, Kawai K (2010) A review of the mechanics of metal spinning. J Mater Process Technol 210:3–23
37. Levy BS, Green DE (2002) Enhanced forming limit diagram. Auto/Steel Partnership, Southfield
38. Emmens WC, van den Boogaard AH (2009) An overview of stabilizing deformation mechanisms in incremental sheet forming. J Mater Process Technol 209:3688–3695
39. Swift H (1948) Plastic bending under tension. Engineering 166:333–359
40. Schleich R, Held C, Sindel M, Liewald M (2009) Investigation on the effect of curvature and sheet thickness on forming limit prediction for aluminium sheet metal alloys. IntJ Mater Form 2:411
41. Huo Q, Yang X, Sun H, Li B, Qin J, Wang J, Ma J (2013) Enhancement of tensile ductility and stretch formability of AZ31 magnesium alloy sheet processed by cross-wavy bending. J Alloys Compd 581:230–235
42. Han T, Huang G, Wang Y, Wang G, Zhao Y, Pan F (2016) Enhanced mechanical properties of AZ31 magnesium alloy sheets by continuous bending process after V-bending. Prog Nat Sci: Mater Int 26:97–102
43. Song D, Zhou T, Tu J, Shi L, Song B, Hu L, Yang M, Chen Q, Lu L (2018) Improved stretch formability of AZ31 sheet via texture control by introducing a continuous bending channel into equal channel angular rolling. J Mater Process Technol 259:380–386
44. Benedyk J, Stawarz D, Parikh N (1971) A method for increasing elongation values for ferrous and nonferrous sheet metals. J Mater 6:16–29
45. Matukhno N, Kljestan N, Knezevic M (2023) Enhancing elongation and trading off strength versus ductility of commercially pure titanium sheets using cyclic bending under tension and annealing. Int J Solids Struct 276:112324
46. Zecevic M, Knezevic M (2023) Origins of improved elongation to fracture in cyclic bending under tension of AA6022-T4 sheets as revealed using crystal plasticity modeling. Mech Mater 177:104546
47. Emmens WC, van den Boogaard AH (2009) Incremental forming by continuous bending under tension—An experimental investigation. J Mater Process Technol 209:5456–5463
48. Poulin CM, Vogel SC, Korkolis YP, Kinsey BL, Knezevic M (2020) Experimental studies into the role of cyclic bending during stretching of dual-phase steel sheets. IntJ Mater Form 13:393–408
49. Roemer TJ, Barrett TJ, Knezevic M, Kinsey BL, Korkolis YP (2019) Experimental study of continuous-bending-under-tension of AA6022-T4. J Mater Process Technol 266:707–714
50. Matukhno N, Kljestan N, Vogel SC, Knezevic M (2022) Cyclic bending under tension of alloy AZ31 sheets: influence on elongation-to-fracture and strength. Mater Sci Eng A 857:144127
51. Knezevic M, Poulin CM, Zheng X, Zheng S, Beyerlein IJ (2019) Strengthening of alloy AA6022-T4 by continuous bending under tension. Mater Sci Eng A 758:47–55
52. Yaddanapudi K, Knezevic M, Mahajan S, Beyerlein IJ (2021) Plasticity and structure evolution of ferrite and martensite in DP 1180 during tension and cyclic bending under tension to large strains. Mater Sci Eng A 820:141536
53. Hosford WF, Caddell RM (2011) Metal forming: mechanics and metallurgy. Cambridge University Press, New York, USA
54. Barrett TJ, Knezevic M (2019) Deep drawing simulations using the finite element method embedding a multi-level crystal plasticity constitutive law: experimental verification and sensitivity analysis. Comput Methods Appl Mech Eng 354:245–270
55. Barlat F, Glazov M, Brem J, Lege D (2002) A simple model for dislocation behavior, strain and strain rate hardening evolution in deforming aluminum alloys. Int J Plast 18:919–939
56. Coppieters S, Cooreman S, Sol H, Van Houtte P, Debruyne D (2011) Identification of the post-necking hardening behaviour of sheet metal by comparison of the internal and external work in the necking zone. J Mater Process Technol 211:545–552
57. Emmens W, van den Boogaard AH (2012) Material characterization at high strain by adapted tensile tests. Exp Mech 52:1195–1209
58. Poulin CM, Barrett TJ, Knezevic M (2020) Inferring post-necking strain hardening behavior of sheets by a combination of continuous bending under tension testing and finite element modeling. Exp Mech 60:459–473
59. Barrett TJ, Knezevic M (2020) Modeling material behavior during continuous bending under tension for inferring the post-necking strain hardening response of ductile sheet metals: application to DP 780 steel. Int J Mech Sci 174:105508
60. Abedini A, Butcher C, Nemcko MJ, Kurukuri S, Worswick MJ (2017) Constitutive characterization of a rare-earth magnesium alloy sheet (ZEK100-O) in shear loading: studies of anisotropy and rate sensitivity. Int J Mech Sci 128–129:54–69
61. Vasilev E, Ferreri NC, Decker R, Beyerlein IJ, Knezevic M (2020) Strain-rate Sensitivity, Tension-Compression asymmetry, r-Ratio, Twinning, and texture evolution of a rolled Magnesium Alloy Mg-1.3Zn-0.4Ca-0.4Mn. Metall Mater Trans A 51:3858–3868
62. Risse M, Lentz M, Fahrenson C, Reimers W, Knezevic M, Beyerlein IJ (2017) Elevated temperature Effects on the Plastic Anisotropy of an extruded Mg-4 wt pct Li Alloy: experiments and Polycrystal modeling. Metall Mater Trans A 48:446–458
63. Mokdad F, Chen DL (2015) Strain-controlled low cycle fatigue properties of a rare-earth containing ZEK100 magnesium alloy. Mater Des 67:436–447

64. Leu B, Savage DJ, Wang J, Alam ME, Mara NA, Kumar MA, Carpenter JS, Vogel SC, Knezevic M, Decker R, Beyerlein IJ (2020) Processing of dilute Mg–Zn–Mn–Ca Alloy/Nb multilayers by accumulative roll bonding. Adv Eng Mater 22:1900673
65. (2015) ASTM E8/E8M-15a Standard Test Methods for Tension Testing of Metallic Materials ASTM International, West Conshohocken, PA
66. Gribbin S, Bicknell J, Jorgensen L, Tsukrov I, Knezevic M (2016) Low cycle fatigue behavior of direct metal laser sintered Inconel alloy 718. Int J Fatigue 93(Part 1):156–167
67. Ghorbanpour S, Bicknell J, Knezevic M (2022) Fatigue strength of additive manufactured Mar-M-509 superalloy. Mater Sci Eng A 840:142913
68. Ghorbanpour S, McWilliams BA, Knezevic M (2020) Effects of environmental temperature and sample pre-straining on high cycle fatigue strength of WE43-T5 magnesium alloy. Int J Fatigue 141:105903
69. Barrett TJ, Takagi S, Islam N, Kuwabara T, Hassan T, Kinsey BL, Knezevic M, Korkolis YP (2021) Material modeling and simulation of continuous-bending-under-tension of AA6022-T4. J Mater Process Technol 287:116658
70. Wenk H-R, Lutterotti L, Vogel S (2003) Texture analysis with the new HIPPO TOF diffractometer. Nucl Instrum Methods Phys Res A Accel Spectrom Detect Assoc Equip 515:575–588
71. Wenk H-R, Lutterotti L, Vogel S (2010) Rietveld texture analysis from TOF neutron diffraction data. Powder Diffr 25:283–296
72. Ferreri NC, Vogel SC, Knezevic M (2020) Determining volume fractions of γ, γ′, γ″, δ, and MC-carbide phases in Inconel 718 as a function of its processing history using an advanced neutron diffraction procedure. Mater Sci Eng A 781:139228
73. Bhowmik S, Zhang J, Vogel SC, Nene SS, Mishra RS, McWilliams BA, Knezevic M (2022) Effects of plasticity-induced martensitic transformation and grain refinement on the evolution of microstructure and mechanical properties of a metastable high entropy alloy. J Alloys Compd 891:161871
74. Bachmann F, Hielscher R, Schaeben H (2010) Texture analysis with MTEX–free and open source software toolbox. Solid State Phenom 160:63–68
75. Bong HJ, Hu X, Sun X, Ren Y (2019) Mechanism-based constitutive modeling of ZEK100 magnesium alloy with crystal plasticity and in-situ HEXRD experiment. Int J Plast 113:35–51
76. Habib SA, Khan AS, Gnäupel-Herold T, Lloyd JT, Schoenfeld SE (2017) Anisotropy, tension-compression asymmetry and texture evolution of a rare-earth-containing magnesium alloy sheet, ZEK100, at different strain rates and temperatures: experiments and modeling. Int J Plast 95:163–190
77. Korla R, Chokshi AH (2010) Strain-rate sensitivity and microstructural evolution in a Mg–Al–Zn alloy. Scr Mater 63:913–916
78. Watanabe H, Ishikawa K (2009) Effect of texture on high temperature deformation behavior at high strain rates in a Mg–3Al–1Zn alloy. Mater Sci Eng A 523:304–311
79. Ulacia I, Dudamell NV, Gálvez F, Yi S, Pérez-Prado MT, Hurtado I (2010) Mechanical behavior and microstructural evolution of a mg AZ31 sheet at dynamic strain rates. Acta Mater 58:2988–2998
80. Poulin CM, Korkolis YP, Kinsey BL, Knezevic M (2019) Over five-times improved elongation-to-fracture of dual-phase 1180 steel by continuous-bending-under-tension. Mater Des 161:95–105
81. Lambri OA, Riehemann W, Trojanová Z (2001) Mechanical spectroscopy of commercial AZ91 magnesium alloy. Scr Mater 45:1365–1371
82. Feather WG, Savage DJ, Knezevic M (2021) A crystal plasticity finite element model embedding strain-rate sensitivities inherent to deformation mechanisms: application to alloy AZ31. Int J Plast 143:103031
83. Feather WG, Ghorbanpour S, Savage DJ, Ardeljan M, Jahedi M, McWilliams BA, Gupta N, Xiang C, Vogel SC, Knezevic M (2019) Mechanical response, twinning, and texture evolution of WE43 magnesium-rare earth alloy as a function of strain rate: experiments and multi-level crystal plasticity modeling. Int J Plast 120:180–204
84. Lentz M, Klaus M, Beyerlein IJ, Zecevic M, Reimers W, Knezevic M (2015) In situ X-ray diffraction and crystal plasticity modeling of the deformation behavior of extruded Mg–Li–(Al) alloys: an uncommon tension–compression asymmetry. Acta Mater 86:254–268
85. Lentz M, Klaus M, Wagner M, Fahrenson C, Beyerlein IJ, Zecevic M, Reimers W, Knezevic M (2015) Effect of age hardening on the deformation behavior of an Mg–Y–Nd alloy: In-situ X-ray diffraction and crystal plasticity modeling. Mater Sci Eng A 628:396–409